PCCP

PAPER

View Article Online
View Journal | View Issue

Cite this: *Phys. Chem. Chem. Phys.*, 2016, **18**, 31586

Chemical vapor deposition-prepared sub-nanometer Zr clusters on Pd surfaces: promotion of methane dry reforming†

Lukas Mayr,[ab] Xue-Rong Shi,[a] Norbert Köpfle,[a] Cory A. Milligan,[bc] Dmitry Y. Zemlyanov,[b] Axel Knop-Gericke,[d] Michael Hävecker,[d] Bernhard Klötzer[a] and Simon Penner*[a]

Received 20th October 2016,
Accepted 8th November 2016

DOI: 10.1039/c6cp07197j

www.rsc.org/pccp

An inverse Pd–Zr model catalyst was prepared by chemical vapor deposition (CVD) using zirconium-*t*-butoxide (ZTB) as an organometallic precursor. Pd–Zr interaction was then investigated with focus on the correlation of reforming performance with the oxidation state of Zr. As test reactions, dry reforming of methane (DRM) and methanol steam reforming (MSR) were chosen. Depending on treatments, either ZrO_xH_y or ZrO_2 overlayers or Zr as sub-nanometer clusters could be obtained. Following the adsorption of ZTB on Pd(111), a partially hydroxylated Zr^{4+}-containing layer was formed, which can be reduced to metallic Zr by thermal annealing in ultrahigh vacuum, leading to redox-active Zr^0 sub-nanometer clusters. Complementary density functional theoretical (DFT) calculations showed that a single layer of ZrO_2 on Pd(111) can be more easily reduced toward the metallic state than a double- and triple layer. Also, the initial and resulting layer compositions greatly depend on gas environment. The lower the water background partial pressure, the faster and more complete the reduction of Zr^{4+} species to Zr^0 on Pd takes place. Under methanol steam reforming conditions, water activation by hydroxylation of Zr occurs. In excess of methanol, strong coking is induced by the Pd/ZrO_xH_y interface. In contrast, dry reforming of methane is effectively promoted if these initially metallic Zr species are present in the pre-catalyst, leading to a Pd/ZrO_xH_y phase boundary by oxidative activation under reaction conditions. These reaction-induced active sites for DRM are stable with respect to carbon blocking or coking. In essence, Zr doping of Pd opens specific CO_2 activation channels, which are absent on pure metallic Pd.

1. Introduction

ZrO_2 is commonly regarded as a highly stable, "irreducible" refractory oxide. Nevertheless, it is currently under investigation to expand its applicability as a catalyst for selective aldehyde oxidation.[1] Regarding CO hydrogenation, the roles of different zirconia polymorphs in the synthesis of higher alcohols were studied both over pure and Pd- or Li-modified ZrO_2.[2] It has also been shown to promote catalysts for methanol reforming processes.[3] In this context, it has been successfully applied as a stabilizing support to prevent CuO_x nanoparticles from sintering, and therefore enhances the stability of methanol steam reforming catalysts.[4] Zr^{4+} ions have also been reported to play an important role as dopants in an Au/CeO_2 catalyst for CO oxidation[5] and in sol–gel-synthesized photocatalysts.[6] Interest in the chemical properties of ZrO_2 polymorphs also arises from its application as YSZ (yttrium-stabilized zirconium oxide), the standard electrolyte for solid oxide fuel cells, due to its electric insulation properties and permeability for O^{2-} ions.[7]

Atomic layer deposition (ALD), or in its general form chemical vapor deposition (CVD), has been already successfully applied for ZrO_2. There are many precursor/oxidative agent pairs known to generate ZrO_2 layers,[8] with the main application as protection/coating layers. Applications beyond catalysis can also be found in microelectronics, where-prepared ZrO_2 was used on SiO_2 as an additional insulation layer.[9] The synthesis of metallic Zr *via* the ALD/CVD pathway from metal–organic precursors to form, by sophisticated activation, nanoparticles

[a] *Institute of Physical Chemistry, University of Innsbruck, Innrain 80-82, Innsbruck, Austria. E-mail: simon.penner@uibk.ac.at; Tel: +43 512 507 58003*
[b] *Birck Nanotechnology Center, Purdue University, 1205 West State Street, West Lafayette, IN 47907, USA*
[c] *School of Chemical Engineering, Purdue University, West Lafayette, Indiana, 47907, USA*
[d] *Department of Inorganic Chemistry, Fritz-Haber-Institute of the Max-Planck-Society, Faradayweg 4–6, D-14195 Berlin, Germany*

† Electronic supplementary information (ESI) available: Overview of XPS Overlayer model, Zr 3d core level region showing *in situ* CVD growth monitored at 673 K, C 1s and Zr 3d core level regions of molecularly adsorbed ZTB, summary of ZTB HREELS peak assignments, HREELS spectra of ZTB decomposition, X-ray diffractograms, MSR reaction profiles. See DOI: 10.1039/c6cp07197j

for catalysis, has – to our knowledge – not been documented sufficiently. Due to the very high formation enthalpy of ZrO_2, special preparation techniques for metallic Zr have been developed,[10] with the aim to control problems of partial oxidation induced by the strong ''getter'' effect of Zr^0. Therefore, CVD from zirconium-*tert*-butoxide (ZTB) was chosen in the present study as an easily applicable, reliable and effective way to prepare ZrO_xH_y overlayers on Pd. The as-prepared CVD layers are not metallic, but contain partially oxidized and partially hydroxylated Zr^{4+} species, which nevertheless, can be easily reduced on Pd to Zr^0 by means of an UHV-based post-treatment. Increased interest in Zr^0-based pre-catalysts also arises from the fact, that oxidative segregation of initially bimetallic surfaces under reaction conditions was recently shown to yield active and selective inverse model catalysts.[11] Such bimetallic pre-catalysts therefore represent a promising approach to obtain strongly enhanced activities (with respect to surface area) as compared to the related supported powder catalytic systems. The enhancement of surface-specific rates can be assigned to the extremely high number of metal-oxide phase boundary sites induced by localized oxidative segregation starting from an atomically dispersed alloy or intermetallic initial state. One of these examples is the initially bimetallic Cu–Zn system. Starting from a dilute Zn-in-Cu alloy, finely dispersed zinc-(hydr)oxide islands are formed *in situ*, leading to a maximum of Cu/ZnO_xH_y phase boundary sites.[12] Thus, an extremely active and selective ''inverse'' MSR catalyst is obtained. The same effect was shown for Cu–Zr, where metallic Zr was sputter-prepared on a Cu substrate and was oxidized/hydroxylated under MSR conditions, yielding phase boundary sites with equally improved CO_2-selectivity and activity.[11]

Two distinct test reactions, methanol steam reforming and dry reforming of methane were chosen to investigate a potential co-catalytic and/or promotional function of surface-near Zr^0-dopants on Pd. Although MSR is an efficient way to generate CO-depleted H_2, catalyst stability issues and the required minimized CO content of the reformate gas make it still an intensely investigated reaction.[4] Cu-based catalysts are known to be excellent to obtain high CO_2-selectivity and high reaction rates,[12] but also Pd-based intermetallic systems are promising due to the methanol-activating function of Pd.[13] As a test reaction, MSR is useful to substantiate and quantify the low-temperature water activation activity of the investigated catalyst systems, because of the fact that CO_2 can only be formed *via* the reaction of activated methanol to formaldehyde, which further reacts with weakly bound –OH species from activated water toward CO_2.

Dry reforming of methane (DRM) is a relevant reaction for the one-step conversion of two climate-relevant greenhouse gases, CO_2 and CH_4, to useful syngas. It is performed at higher temperatures ($\sim$970 K) than MSR and does not so much rely on initial water- but rather on CO_2-activation. It is usually initiated by methane decomposition toward different carbon species. If the latter are sufficiently reactive, they can be further converted *via* the subsequent Boudouard reaction to CO, or else, they remain deposited as unreactive coke. However, also the inverse water-gas-shift reactivity of the catalyst may play a role,[14] either as an additional intermediate process to generate water, which may be important for efficient gasification of carbon deposits, or as an unwanted side reaction reducing the H_2 yield. Transition metals such as Co, Ni, Ru, Rh, Ir and Pt on alumina and silica supports[15,16] have been reported as efficient DRM catalysts. Ceria as a support for Ni and Co was also applied,[13] but also mixed ceria and zirconia supports.[17] Clean Pd is known for its pronounced methane- but simultaneously quite poor CO_2-activation ability. Therefore, DRM was chosen as a reference reaction to investigate the promotion of CO_2 activation on a Zr-doped inverse Pd model catalyst, in order to highlight the role of the eventual initial Zr^0 nanoclusters for enhanced CO_2 activation.

The main goal of this inverse model catalyst study is therefore to highlight the co-catalytic/promotional role of redox-active Zr surface species on Pd beyond the simple function of zirconia as a structurally stabilizing catalyst support. As will be shown in the following, Zr^0 clusters of 2–6 atoms adsorbed on Pd can be oxidized, reduced or hydroxylated reversibly at comparably low temperatures around 723 K. Beyond the redox properties, electronic structure nano-effects of small particles and surface islands have also been described for other elements, *i.e.* gold on TiO_2,[14,15,18,19] which may alter the catalytic properties substantially. Zr, in its nanostructured highly redox-active surface-adsorbed state, is therefore investigated to be part of a potential redox active cycle and to open new reaction pathways on chemically and electronically altered Pd.

2. Experimental and computational methods

Depending on the experimental requirements, the research was performed using three experimental setups: An Omicron Surface Analysis Cluster (Birck Nanotechnology Center at Purdue University), an UHV-chamber with attached high-pressure recirculating batch reactor, and the Innovative Station for *in situ* Spectroscopy (Beamline ISISS at BESSY II synchrotron in Berlin).

2.1. Omicron setup

The Omicron Surface Analysis Cluster consists of a UHV preparation chamber and an analysis chamber with base pressures of 1×10^{-9} mbar and 5×10^{-11} mbar, respectively. Samples can be transferred between these chambers under UHV. The preparation chamber is equipped with a mass spectrometer, an Ar^+ sputtering gun, a gas manifold system, and resistive sample heating. The analysis chamber is equipped with X-ray Photoelectron Spectroscopy (XPS) (electron energy analyzer – Omicron EAC 125 and analyzer controller – Omicron EAC 2000), Low Energy Electron Diffraction (LEED) (Omicron), High Resolution Electron Energy Loss Spectroscopy (HREELS) (ELS5000, LK Technologies), Scanning Tunneling Microscopy (STM) (Omicron ambient temperature UHV STM/AFM), and resistive sample heating. XPS data are acquired using a non-monochromatic Mg Kα X-ray source ($h\nu$ = 1253.6 eV) at 150 W. High resolution spectra are recorded

at the constant pass energy of 20 eV. Photoelectrons are ejected at a 45° angle with respect to the surface normal.

The Pd(111) single crystal (orientation accuracy $<0.1^{\circ}$, Princeton Scientific) is cleaned by several cycles of Ar^{+}-sputtering (1 kV, 2 μA sample ground current) and annealing to 900–1000 K until no contaminations could be detected by XPS, STM and LEED. Well-ordered monoatomic steps are seen in STM. Due to the potential impact of radiation of the X-ray source on the sample topography/chemistry, STM studies are always done before XPS characterization. Sample heating is performed in the analysis chamber.

Zirconium(IV) *tert*-butoxide $Zr(O\text{-}t\text{-}C_4H_9)_4$ (Strem, purity: 99%) is used as ALD/CVD precursor and filled into an cylinder under Ar. Prior to dosing ZTB, several cycles of freeze–pump–thaw are performed for purification (cooling temperature: 223 K, freezing point ZTB: 269 K). ZTB has a sufficient vapor pressure at room temperature to dose it directly through a leak-valve. Before sample exposure, the preparation chamber is exposed to the precursor at 5×10^{-7} mbar for 5 minutes to passivate the chamber walls against precursor decomposition. The exposure is calculated from uncorrected ion gauge measurements in Langmuir, ($1\ L = 1 \times 10^{-6}$ Torr s) involving exposure pressures in the range of 5×10^{-8} to 5×10^{-6} mbar. The adsorbate coverage is determined from XPS data (details can be found in the XPS experimental section or additionally in ref. 20–23).

2.2. UHV-chamber with attached high-pressure recirculating batch reactor

Sample preparation and characterization was performed in a combined preparation/analysis chamber with attached reaction cell, described in more detail elsewhere (base pressure in the low 10^{-9} mbar range).[24] The sample is heated *via* a home-built e-bombardment setup. Electrons are ejected from a triple-filament emitter (operated with 30 W heating power) set to −500 V, while the sample is set to +300 V. The electron impact heating power is controlled *via* the filament emission current. For spectroscopic analysis, the chamber is equipped with a hemispherical electron and ion analyzer (Thermo Fisher Electron Alpha 110), a double anode X-ray gun for XPS (Mg/Al, XR 50, Specs), an ion gun sufficient to produce 1 kV He^{+} ions for ISS (Omicron 100) and an electron beam gun for Auger electron spectroscopy (KPI EGPS-2017B). Additionally, a mass spectrometer (Balzers) for residual gas analysis and an Ar^{+} ion sputter gun for sample cleaning is attached. A three way gas inlet allows to dose O_2 (Messer, 5.0), H_2 (Messer 5.0) or O_2 cleaned Ar (Messer 5.0) *via* leak valves into the chamber. All XPS spectra in this chamber are recorded with a non-monochromatic Mg Kα X-ray source ($h\nu$ = 1253.6 eV) at 250 W and at the magic angle to the analyzer. For XPS the analyzer is operated at a constant pass energy of 20 eV.

All catalytic experiments are performed using a 20 × 18 mm ultra-clean polycrystalline Pd foil (Goodfellow, 99.95%) with a thickness of 0.125 mm. For reference experiments on pure ZrO_2, a pre-oxidized 0.127 mm Zr foil with the same size (Alfa Aesar, purity: 99.95%) is used. The foils are cleaned before loading to the UHV chamber in a water and an ethanol ultrasonic bath for 20 min, respectively. ZTB (Sigma Aldrich, purity. 99.999%) is filled and mounted to the combined preparation/analysis chamber as described for the Omicron setup above. ZTB exposition is performed as described in the context of the individual experiments discussed below. Sample heating is performed by electron impact heating.

In order to validate the CVD-based catalytic results and to obtain a broader experimental basis of the Pd–Zr^0 system with respect to reforming performance, also an intermetallic bulk phase of Pd and Zr^0 is prepared. The preparation is performed under HV conditions (base pressure 1×10^{-7} mbar) by heating small pieces of the above-specified pure Pd and Zr foil samples resistively in a Ta crucible in the nominal atomic ratio 2 : 1. At a temperature slightly above the melting point of Pd (1828 K), spontaneous reaction between Pd and Zr leads to an intermetallic Pd–Zr melt, which then recrystallizes toward Pd–Zr bulk phases during cooling in vacuum. Thereafter, this sample is transferred to the UHV system with attached batch reactor for analysis and catalytic testing. Note, that this sample, in comparison to the CVD-prepared ones, is exposed to air at room temperature between preparation and characterization. The nominal 2 : 1 Pd : Zr stoichiometry (*i.e.* with Pd excess) is chosen with the idea to maintain at least some active Pd metal surface coexisting with oxidatively segregated Zr species under reaction conditions. Moreover, an excess of Pd is necessary because the melting point of Zr is very high and complete intermetallic formation reaction of Pd with Zr is necessary in order to distribute the Zr^0 homogeneously in the melt. The corresponding X-ray diffraction patterns of the initial Pd–Zr sample is made up by a complex superposition of at least two different Pd–Zr intermetallic phases, including Pd_3Zr and Pd_4Zr_3, alongside a small amount of oxidized monoclinic ZrO_2. Note that this is in striking contrast to the similarly prepared Cu–Zr samples,[24] indicating a much less initial homogeneous melt. In due course, as will be discussed below, after the DRM reaction, the patterns are even more complicated, indicating phase transformations and partial (oxidative) decomposition of the intermetallic Pd–Zr compounds.

For catalytic testing in the ambient pressure recirculating batch reaction cell, a long z-transfer rod allows fast and reliable transfer without exposure to air. The all-quartz-glass high-pressure (up to 1 bar) batch reactor is equipped with a gas chromatograph with either intermediate or continuous EID-MS detection to determine the exact gas composition at any point of reaction. Continuous partial pressure detection is performed *via* a capillary leak to the GC-MS. The quartz-glass reactor with a total circulation volume of 296 ml is designed to measure small reaction rates and selectivity patterns within a temperature range between room temperature and 1300 K. A circulation pump ensures a constant flow and gas intermixing and an attached gas-premixing unit allows to set arbitrary compositions of the attached reactant vapors or introduced gases (methanol, methane (5.0), deionized and degassed water, CO_2 (5.0), O_2 (5.0), H_2 (5.0), Ar (5.0) and He (5.0). The sample holder itself is entirely made of quartz glass to avoid background reactivity from hot metal parts and is designed for 20 mm × 18 mm metal foils.

A partial pressure of 8–30 mbar argon added to all gas mixtures allows to account for the thermal expansion due to the temperature increase and the simultaneous gas loss through the capillary leak for continuous EID-MS detection. For partial pressure calculations, all base-line-corrected MS signals are calibrated using pure substances with quantitative consideration of fragmentation. For all MSR catalytic experiments shown in this work, the following initial conditions are applied: 12 mbar methanol, 24 mbar water, 8 mbar argon, He added to a total pressure of 1 bar. After an equilibration and premixing period of 10 min, a heating routine (rate 10 K min^{-1}) up to 623 K is performed, followed by an isothermal period at 623 K. For all DRM catalytic experiments shown in this work, 50 mbar methane, 50 mbar CO_2, 30 mbar Ar, adding He added to a total pressure of 1 bar were chosen. After an equilibration and premixing period of 10 min, a temperature ramp up to 1073 K within 30 min was performed, followed by a corresponding isothermal period at 1073 K. For discussion about mass and heat transport limitations, we refer to a thorough discussion of the catalytic setup in ref. 25.

2.3. *In situ* XPS setup

Synchrotron-based *in situ* XPS experiments were performed at the ISISS (Innovative Station for *in situ* Spectroscopy) beamline at the BESSY II synchrotron in Berlin, Germany. The experimental apparatus consists of a load lock and an *in situ* cell connected to the XPS spectrometer *via* differential pumping stages. The experimental apparatus has been described in the literature in detail previously.[26] Samples are heated in the *in situ* cell *via* a near-infrared semiconductor laser (λ = 808 nm) from the rear. The temperature is measured by a K-type (chromel–alumel) thermocouple positioned between sample holder back plate and Pd foil. All *in situ* experiments are performed on the same Pd foil sample that is used for the model catalyst preparation in the UHV instrument with attached batch reactor.

The same ZTB cylinder/leak valve setup described above is transferred to ISISS beamline. Due to the fact that ZTB only interacts with surfaces hotter than 500 K, it is safe to dose the organometallic precursor into the analysis chamber without any Zr deposition on the components of the vacuum system or on the X-ray window. The growth of ZTB can then be followed directly *via* XPS. To determine a potential influence of the X-ray beam on the sample structure and chemistry, heating was performed at random checking with and without X-ray beam. As no distinct changes in the spectra between the two runs have been observed, this influence is considered to be marginal.

Monochromator control allows to chose photon energies corresponding to kinetic energies of the ejected photoelectrons of 120 eV for all monitored core-level photoemission peaks in order to extract information from a constant information depth and to yield the same attenuation of the photoelectrons through the gas phase. Due to the fact that 95% of the signal arises from a sample depth up to ~1 nm, this operation mode is considered to be maximum ''surface sensitive''.

Photoelectrons are collected in the direction normal to the surface at constant pass energy of 10 eV. Binding energies were referenced to the Fermi edge, which is measured each time the monochromator moves to a new position (*i.e.* whenever the incident photon energy was changed). Photoemission peak intensities are corrected for the respective photon flux at a given photon energy. Since the BESSY II synchrotron operates in top-up mode (constant ring current), no additional correction for the ring current was required. Since all photoemission peaks were collected at the same kinetic energy of photoelectrons (120 eV), the attenuation through the gas phase was the same for all-core levels and, thus, cancels out in coverage calculations.

2.4. Analysis of the XPS data

All spectra are analyzed using the CasaXPS software program, version 2.3.16 Pre-rel 1.4 (Casa Software Ltd).[27] A Shirley background is applied to all spectra and the associated Scofield relative sensitivity factors are used for quantification. For peak fitting of the Zr 3d peaks a weighted sum of Gaussian and Lorenzian peak shapes (CasaXPS line shape SGL(30)) is assumed, using a doublet separation (Zr $3d_{5/2}$ *vs.* Zr $3d_{3/2}$) of 2.4 eV for both metallic Zr[28] and zirconia[29] was used for fitting. The doublet area is kept constant at 3 : 2 as arising from spin–orbit d-electron coupling. Electron attenuation lengths were taken from the NIST database SR 82[30] and the orbital asymmetric parameter from the ELETTRA online database of ref. 31 The quantification of the XPS data is given as atomic percentages or coverage/thickness. The atomic percentage is estimated assuming homogeneously mixed elements. Since an adlayer on the substrate surface is not a homogeneous system, the coverage/thickness gives a better representation. The ZrO_xH_y surface coverage is calculated assuming a non-attenuating adlayer on a semi-infinite substrate.[20–23] As the maximum ZrO_xH_y layer thicknesses remained in the sub-monolayer regime in this study, the influence of a potential attenuation effect of the photoelectrons by the overlayer remains negligible even for the highest exposures. This is tested by comparing the results on a ~1 ML ZrO_xH_y covered sample, using both an attenuating and non-attenuating overlayer model, which eventually shows negligible differences. Details of these calculations are given in ref. 20–23 and in the ESI,† Section A.

2.5. Density functional theory (DFT)

All calculations are performed with plane-wave DFT using the Vienna *ab initio* simulation package (VASP) using the projector augmented wave (PAW) method.[32,33] To elucidate the role of the van der Waals interaction in this system, we perform vdW-DF calculations using the optB88 functional.[34,35] The cutoff energy for the plane wave basis set is fixed at 400 eV. Geometry optimization is performed with a conjugate-gradient algorithm and considered to be converged when the forces on each unconstrained atom was <0.01 eV $Å^{-1}$. A Monkhorst–Pack grid of $2 \times 2 \times 1$ is employed due to the large unit cell. We use a $\sqrt{7} \times \sqrt{7}$ surface unit cell for Pd(111) with five layers thickness. The bottom two layers are fixed at their bulk position. On top of the Pd surface, 1 to 3 layers of a (2×2) cubic ZrO_2 film are adsorbed and fully optimized. According to the previous

experimental STM observations and theoretical work,[16,17] we take the (111) surface of cubic ZrO_2 as the surface orientation of the ZrO_2 film. The calculated lattice mismatch between each other is 1.3%. The reaction energy ΔE of deposited ZrO_2 films on the Pd surface is calculated by

$$\Delta E = [E_{\text{total}}(\text{ZrO}_2\text{–Pd}) - E_{\text{total}}(\text{Pd}^{\text{surf}}) - n_{\text{ZrO}_2}E_{\text{total}}(\text{ZrO}_2^{\text{bulk}})]/A_{\text{cell}} \quad (1)$$

which is defined by the difference between the total energy of the compound system $[E_{\text{total}}(\text{ZrO}_2\text{–Pd})]$ and the sum of the total energy of the clean Pd surface $[E_{\text{total}}(\text{Pd}^{\text{surf}})]$ and the total bulk energy $[E_{\text{total}}(\text{ZrO}_2^{\text{bulk}})]$ of as many ZrO_2 formula units as are adsorbed within a unit cell on top of the metal surface (n_{ZrO_2}) divided by the area of the two-dimensional unit cell A_{cell}. The smaller the ΔE value, the more stable the structure becomes.

The formation energy of ZrO_2 films with a different number of layers is defined by

$$\Delta E_{\text{film}} = E_{\text{total}}(\text{ZrO}_2) - n_{\text{ZrO}_2}E_{\text{total}}(\text{ZrO}_2^{\text{bulk}}) \quad (2)$$

where $E_{\text{total}}(ZrO_2)$ is the total energy of the relaxed ZrO_2 film. Here the lattice parameters ($a = b$) of the ZrO_2 film and the ion positions are all allowed to change. The adsorption energy of the ZrO_2 film at the Pd(111) surface is then calculated by

$$\Delta E_{\text{ads}} = E_{\text{total}}(\text{ZrO}_2\text{–Pd}) - E_{\text{total}}(\text{Pd}^{\text{surf}}) - E_{\text{total}}(\text{ZrO}_2). \quad (3)$$

From eqn (1)–(3), it follows $\Delta E = (\Delta E_{\text{film}} + \Delta E_{\text{ads}})/A_{\text{cell}}$.

The temperature- and pressure-dependent terms of condensed phases are small and tend to be neglected in the free energy calculation. The differences between the chemical potentials can be approximated by the difference between their calculated DFT electronic energies (E_{total}). For the gas phase, the thermal contributions from the translational, rotational and vibrational enthalpies and entropies are added.[36] By this definition, the reaction energy ΔG_{diss} for oxygen dissolution into Pd sub-layer and ΔG_{diff} for oxygen diffusion to the available bare Pd(111) surface are not affected by the reaction temperature and pressure, and will be equal to the reaction energy at 0 K.

The reaction energy ΔG_{diss} for oxygen dissolution into Pd sub-layer is calculated by

$$\Delta G_{\text{diss}} = E_{\text{total}}(\text{ZrO}_2\text{–O–Pd}) - E_{\text{total}}(\text{ZrO}_2\text{–Pd}). \quad (4)$$

$E_{\text{total}}(ZrO_2–O–Pd)$ is the total energy of ZrO_2–Pd system with one oxygen dissolving into the Pd sub-layer. The reaction energy ΔG_{diff} for oxygen diffusion to the available neighboring bare Pd(111) surface is then calculated by

$$\Delta G_{\text{diff}} = E_{\text{total}}[(\text{ZrO}_2)_{\text{Ovacancy}}\text{–Pd}] + E_{\text{total}}(\text{O–Pd}) - E_{\text{total}}(\text{ZrO}_2\text{–Pd}) - E_{\text{total}}(\text{Pd}^{\text{surf}}). \quad (5)$$

$E_{\text{total}}[(ZrO_2)_{\text{Ovacancy}}–Pd]$ is the total energy of the compound ZrO_2–Pd system with one oxygen vacancy at the ZrO_2 film. $E_{\text{total}}(O–Pd)$ is the total energy of the Pd(111) surface with one adsorbed oxygen atom. All the Pd surfaces here have the same surface area. For the O_2 production in the gas phase, the reaction Gibbs free energy ΔG_{O_2} is calculated by

$$\Delta G_{\text{O}_2} = \Delta E_0 + 0.5G(T) \quad (6)$$

with

$$\Delta E_0 = E_{\text{total}}[(\text{ZrO}_2)_{\text{Ovacancy}}\text{–Pd}] + 0.5E_{\text{total}}(\text{O}_2) - E_{\text{total}}(\text{ZrO}_2\text{–Pd}). \quad (7)$$

ΔE_0 is the reaction energy at 0 K including the zero-point energy evaluating from the difference of the electronic energies between the products and the reactants, and $G(T)$ represents the free energy of O_2 in the gas phase under the chosen experimental reaction temperature and pressure. $E_{\text{total}}[(ZrO_2)_{\text{Ovacancy}}–Pd]$ is the total energy of the compound ZrO_2–Pd system with one oxygen vacancy at the ZrO_2 film.

3. Results

3.1. Synthesis of the starting catalyst structure and redox chemistry of Zr

3.1.1. ZTB adsorption on palladium surfaces and the ALD/CVD window. Following ZTB exposure of Pd(111) at room temperature, only a small amount of zirconium is detected by XPS and only when Pd(111) is pre-treated with oxygen prior to ZTB exposure (2000 L at 298 K; this yields a p(2 × 2) O_{ads}/Pd(111) structure, but no surface Pd oxide, which only forms at elevated temperatures). The coverage of as-deposited ZrO_xH_y is estimated to be in the range of 10^{-2} ML following high exposures of ~2000 L. In order to increase the ZrO_xH_y coverage, we explore an ALD-like approach: multi-cycles of ZTB exposure followed by annealing in UHV. ZTB exposure is performed at room temperature the (first half of the ALD cycle) and annealing in UHV is performed at 673 K (second half of the ALD cycle, no co-reactant). As shown in Fig. 1A, this approach does not help to grow more Zr: no increase of the Zr amount is observed with number of cycles. The carbon coverage is in the range of ~1.5 ML, increasing after ZTB exposure and decreasing after UHV annealing, which also results in removing Zr.

Typically, an ALD/CVD process is characterized by a specific temperature window. For instance, the exposure temperature is recommended to be around 650 K for Si.[9] The ALD window for the decomposition of ZTB on a SiO_2 wafer was between 573 K and 673 K.[37,38] The activation barrier was explained by a hydride elimination step, which was considered as a rate limiting step, and the formation of isobutene.[37] A pure ALD mechanism was supposed to occur below 573 K. We investigated the dependence of the zirconium amount from the ZTB exposure temperature. Fig. 1B shows the amount of zirconium and carbon (in atomic percent for a rough quantitative estimation) calculated from the Zr 3d and C 1s XPS peaks as a function of ZTB exposure temperature. Carbon can be mainly found on the surface following exposure at temperatures below a sharp threshold of ~573 K. Above 573 K, the Zr/Pd ratio increases rapidly and the amount of carbon decreases. A remarkably similar behavior was observed during ZrO_2 growth from ZTB on Si(100) by Cameron and George,[38] where the CVD rate of ZrO_2 increased sharply above 573 K and then started to drop above 773 K. At high temperatures, ZrO_2 deposition was supposed to be partially poisoned by carbon. Fourier transform infrared spectroscopy (FTIR) demonstrated hydroxyl (ZrOH*) and butoxide

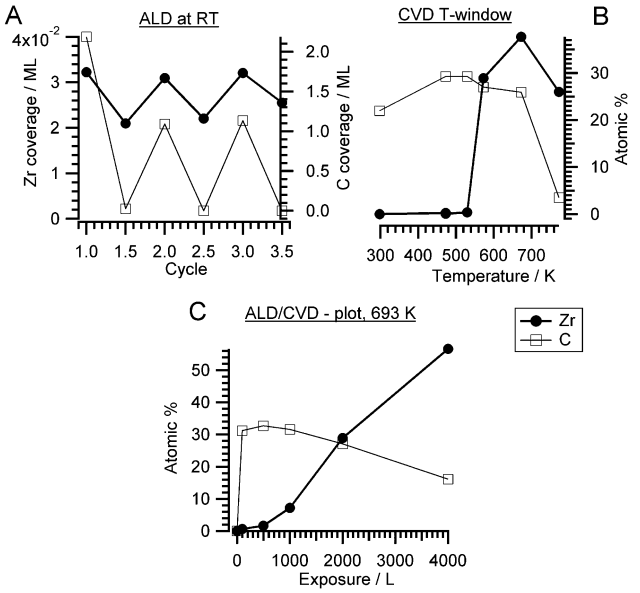

Fig. 1 (A) Zr and C coverage as a function of number of ALD-like cycles: 1st half cycle – 2000 L ZTB adsorption at RT and 2nd half cycle – annealing at 673 K in vacuum. Prior to the first ALD cycle, the clean Pd(111) surface was exposed to 2000 L O_2 at 298 K; (B) constant exposure of 2000 L at selected temperatures, indicating the CVD window. (C) Langmuir plot of Zr and C atomic% derived from Zr 3d, C 1s and Pd 3d *versus* ZTB exposure at 693 K (isothermal conditions).

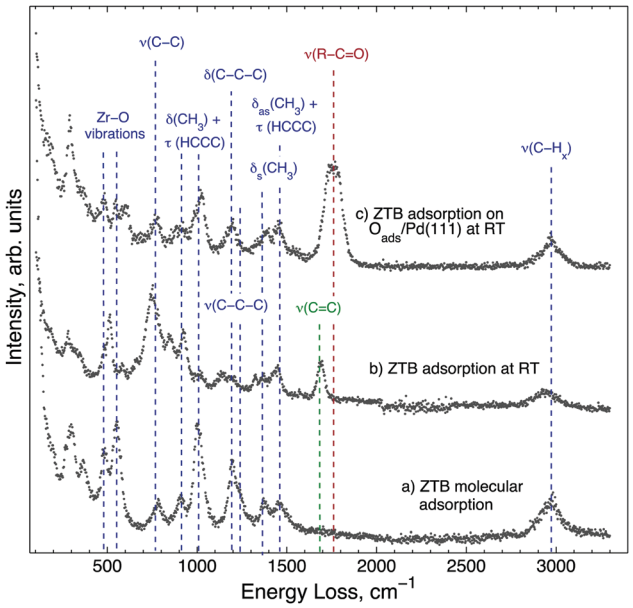

Fig. 2 HREEL spectra obtained following 2000 L ZTB exposure of the Pd(111) surface (a) at 180 K and heated to 293 K in UHV, (b) and (c) at 293 K; for (c), Pd(111) was pre-exposed to 2000 L O_2 at 673 K. HREELS spectra were collected at 293 K. The energy losses, which are characteristic of ZTB, are marked in blue.

($ZrOC(CH_3)_3$*) species on ZrO_2, whose concentration decreased roughly linearly with temperature from 300–800 K.[33] In our case, we do not detect much carbon deposition at high temperatures. However, a much lower ZTB pressure is used in our study ($\sim 10^{-5}$ Torr *vs.* 0.05 Torr in ref. 38) and Pd exhibits a high carbon dissolution capability.[39] Therefore, on Pd the amount of deposited Zr decreases above 673 K most likely due to kinetic limitations: fast desorption of ZTB effectively competes with dissociation. The temperatures between 550–773 K are most efficient for zirconium deposition, more effective than multiple ALD-like cycles at room temperature. The temperature of 693 K is usually used for the CVD experiments described in this study because of the empirically determined trade-off between reducing the unwanted carbon deposition and optimizing the Zr amount.

A Langmuir-type plot (deposited amount of Zr and C *versus* ZTB exposure in Langmuir) obtained at 673 K is shown in Fig. 1C. No zirconium saturation was observed even at 4000 L, while the carbon amount was decreasing with exposure. Increasing with exposure, the Zr amount is more typical for CVD than for ALD. The CVD was also reported for ZTB adsorption on Si(100).[38] Interestingly, carbon is displaced by zirconium compounds, which might reflect a competition for adsorption/dissociation sites between ZTB and its decomposition products (*i.e.* hydrocarbons). ZTB dissociation products could hinder ZTB adsorption and block further ZTB dissociation. A similar situation was observed during trimethylaluminum and ferrocene adsorption on Pd(111) and Pt(111).[21,22] The CVD growth of ZrO_xH_y on Cu is also monitored *in situ*. The corresponding XP spectra are shown in the ESI† in Fig. S1.

In order to identify adsorption species and to understand the low zirconium uptake below 550 K, ZTB adsorption is investigated by HREELS (Fig. 2). Molecularly adsorbed ZTB was prepared by 2000 L exposure on Pd(111) at 180 K and followed by warming up to 293 K (spectrum (a) in Fig. 2). Despite the rather complex spectrum, all detected vibrations are very similar to those detected from FTIR in gas phase for the *tert*-butyl group and ZTB.[40–43] In XPS (ESI,† Fig. S2), two separate C 1s peaks can be seen at 286.9 eV and 284.9 eV following ZTB exposure, which can be attributed to carbon bound to oxygen or carbon, respectively. By comparison with the Zr $3d_{5/2}$ peak area, the C/Zr ratios for the oxygenated and non-oxygenated species are 4.9 and 17.4, respectively. This allows us to conclude that adsorption of ZTB is mostly molecular under these conditions. The characteristic frequencies of ZTB on Pd(111) are summarized in the ESI† in Table S2 and compared with literature values. The HREELS spectrum obtained following ZTB adsorption on Pd(111) at 293 K (spectrum (b) in Fig. 2) is slightly different. The main difference is a new peak at 1685 cm^{-1} (marked dark-green). This peak can be assigned to the stretching of the double C=C bond,[44–46] which most likely is due to adsorbed isobutylene species. Indeed, thermal desorption of isobutylene correlated with the ZrO_2 growth rate,[38] and this observation along with FT-IR-detected butoxide species ($ZrOC(CH_3)_{3,ads}$) allowed Cameron and George[38] to conclude that the butoxide species decomposition *via* β-hydride elimination is the rate-limiting step for ZrO_2 film growth. This conclusion is consistent with our HREELS data showing dissociation of ZTB and the appearance of the adsorbed isobutylene species. The intensity enhancement of a skeletal vibration of *tert*-butyl group, ν(C–C), at 780 cm^{-1} infers

that the surface is covered with ZTB dissociation products. The C/Zr ratio increased compared to the molecular adsorption as well. The ratio for the room temperature-exposure roughly is 30 : 1 atomic% C : Zr. Thus, hydrocarbon products of ZTB dissociation "passivate" the Pd(111) surface against further ZTB adsorption.

Spectrum (c) in Fig. 2 was obtained following 2000 L ZTB exposure of Pd(111) covered by O_{ads}. Interestingly, the spectrum is close to the one for the molecular adsorption of ZTB (spectrum (a), Fig. 2): it is likely that the surface contains less ZTB dissociation products, as no adsorbed isobutylene species are found on the surface. On the other hand, a new peak appeared at 1745–1775 cm^{-1} (dark-red), which can be due to a C–O stretching vibration in aldehyde or ketones.[44–46] Likely, an isobutyl fragment splitting off ZTB could attach to a surface oxygen center without β-hydride elimination. No OH vibration following ZTB adsorption in all three cases is observed.

According to the HREELS data, even slight heating of ZTB adlayers in UHV resulted in decomposition of hydrocarbon species (ESI,† Fig. S3). Structure-wise, following adsorption of 100 L ZTB at 673 K, the surface is covered with a layer of rather disordered ZrO_x mixed with carbon as determined from STM images (Fig. 3A). This layer is not uniform and contains holes and cracks (Fig. 3B). The surface carbon species seen in this stage are most likely C_xH_y fragments and/or graphitic deposits, as deduced from the main C 1s components around 284 eV (not shown). A relatively broad height distribution within the terraces (not shown) indicates the limited uniformity of the overlayer.

Based on the data discussed above, we propose the following mechanism of ZTB–Pd surface interaction.

On clean Pd(111), ZTB dissociates *via* β-hydride elimination, resulting in adsorbed isobutylene and butoxide ($ZrOC(CH_3)_{3,ads}$) species. Isobutylene species either desorb as isobutylene or decompose and hydrogenate leaving carbon on the surface.

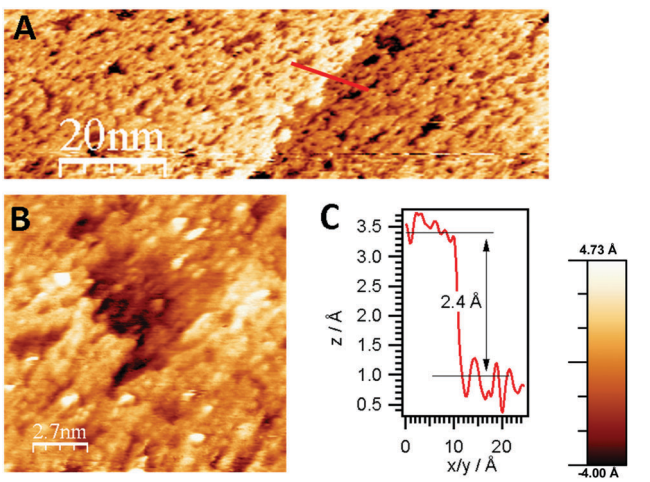

Fig. 3 (A) STM images of the CVD-grown ZrO_x overlayer on Pd(111) (100 L ZTB at 673 K, ZrO_xH_y–carbon layer coverage estimated to ~1 ML, bias voltage: −0.8 V, tunneling current: 0.4 nA), including monoatomic step edge profile in the Pd(111) surface, (B) crack in the non-uniform mixed ZrO_xH_y + carbon overlayer, C) height profile of step edge along the line shown in A.

The adsorbed butoxide species dissociates further, resulting in ZrO_x deposition (* denoting an adsorption site, n and x are stoichiometric factors):

$$Zr(OC_4H_9)_4 + n^* \rightarrow Zr(OC(CH_3)_3)_{x,ads} + (4-x)CH_2{=}CH{-}(CH_3)_{2,ads} + (4-x)O_{ads} \quad (x = 1, 2 \text{ and } n = 7, 5) \qquad (R1)$$

$$Zr(OC(CH_3)_3)_{x,ads} + x^* \rightarrow ZrO_x + xCH_2{=}CH{-}(CH_3)_{2,ads} \qquad (R2)$$

$$CH_2{=}CH{-}(CH_3)_{2,ads} \rightarrow CH_2{=}CH{-}(CH_3)_2\uparrow + * \qquad (R3)$$

$$CH_2{=}CH{-}(CH_3)_{2,ads} + 3^* \rightarrow 4H_2\uparrow + 4C \qquad (R4)$$

$$ZrO + O_{ads} \rightarrow ZrO_2 + *. \qquad (R5)$$

As dissolution of carbon atoms in Pd is fast above 573 K on Pd,[39] we assume this process to dominate the ALD vacuum annealing step. Some oxygen could be consumed for hydrogen and carbon oxidation. The further fate of ZrO_2 is discussed separately. We can conclude that at temperatures below the threshold of ~550 K, the surface is poisoned by carbon compounds and above 773 K, the deposition rate starts to decline due to kinetic limitations (too fast desorption of ZTB).

On O_{ads}/Pd(111), the main difference is the appearance of alkoxide-like species showing C=O stretching vibrations. The exact configuration of this species is out of this work's scope and would require further investigation.

3.1.2. Reduction and oxidation of Zr-containing species on Pd surfaces. Annealing in vacuum at 673 K removes carbon efficiently (structure Fig. 4, XP spectra shown in Fig. 5). Surprisingly, annealing for 10 min results in zirconium reduction to Zr^0: the Zr $3d_{5/2}$ peak shifts from 183.15 eV for the precursor (Zr^{4+}) to 179.6 eV, which is formally Zr^0. This is a remarkable finding, since bulk zirconia is a very stable oxide and the reduction of bulk phases of this oxide without intimate contact to a noble metal is only possible under extremely harsh conditions. The oxide formation enthalpy is −1100 kJ mol^{-1}.[47] In fact, it is usually very hard to even keep Zr in its metallic state. Fig. 4 shows the STM images obtained following 100 L ZTB exposure of Pd(111) at 673 K and annealing in UHV at 723 K. According to XPS, carbon is largely removed, and STM detects evenly-distributed sub-nanometer clusters with the height of ~0.4 nm, corresponding to a monoatomic height step of zirconium. Note that in the images, most likely a double tip along the scan direction is present, which doubles the present Zr atom clusters. However, the 1–3 atom clusters (blue framed) were assigned to metallic Zr. The atom-atom distance between two neighbouring elemental Zr^0 atoms not being affected by the double tip amounts to 0.32 nm (hcp lattice), and does, thus, fit to a certain degree to the dimensions of the Pd arrangement of the Pd(111) surface, exhibiting a Pd–Pd distance of 0.28 nm between nearest neighboring atoms. The large misfit of the interatomic distances for Pd(111) and Zr(0001) likely prevents epitaxial growth of Zr on Pd(111).

The unusual behavior on Pd under vacuum conditions, leading to the formation of nanostructured Zr^0 islands, is explained by efficient removal of oxygen atoms and an extremely low re-oxidation rate. As deduced from STM images and DFT

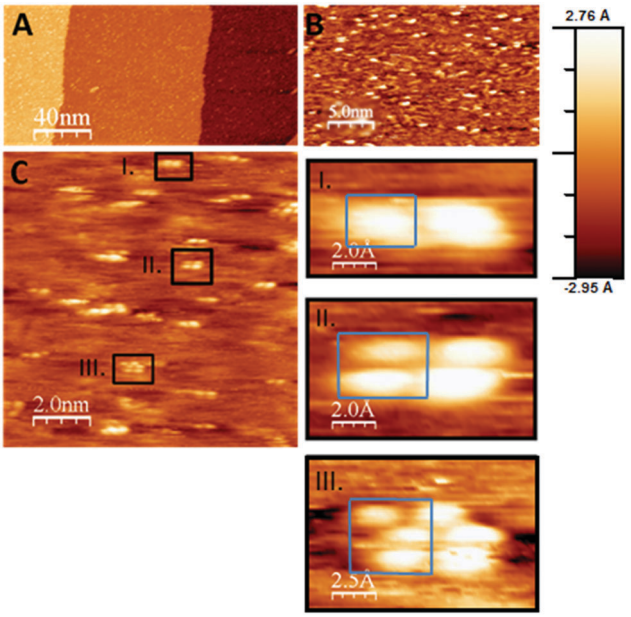

Fig. 4 (A–C) STM images obtained after CVD growth of the ZrO_xH_y + C overlayer (100 L ZTB at 673 K) on Pd(111) followed by UHV-annealing to 723 K in 5×10^{-11} mbar. The resulting Zr^0 coverage was ~0.1 ML, and no more carbon was detected after annealing. The formed Zr-nanoclusters are shown in panel C and sub-panels I–III. (gap voltage: 0.2 V, constant current mode, feedback setting: 0.2 nA). Clusters containing 1–3 Zr atoms (blue frames) are seen (note that the structure most likely is imaged using a double tip. However, as all structural features seem to be doubled along the scan direction, the clusters containing 1–3 Zr atoms seen along the direction almost perpendicular to it are true Zr clusters being present on the surface).

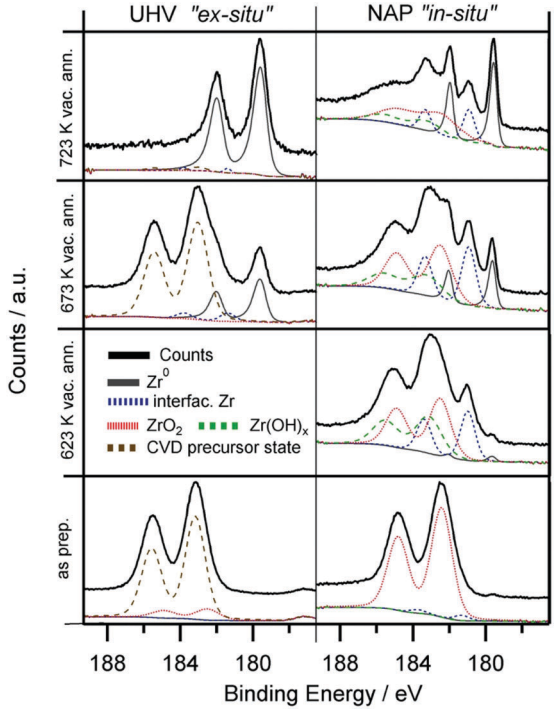

Fig. 5 Zr 3d spectra of the CVD-grown ZrO_xH_y overlayer (673 K, 2000 L ZTB) at room temperature ("as prepared") and after annealing in vacuum to 623 K, 673 K and 723 K. Left panels: experiments on Pd(111), base pressure of the UHV XPS chamber 5×10^{-11} mbar. Right panels: experiments on a Pd foil at the NAP-XPS setup of ISISS beamline at HZB/BESSY II, base pressure 5×10^{-8} mbar. The initial Zr coverage for both experiments is approximately 0.6 ML.

calculations shown later, metal support interaction effects are also highly beneficial. Even though a number of Pd–Zr intermetallic bulk phases and/or compounds of varying stoichiometry are known,[47,48] no such Pd–Zr phases can be formed at temperatures as low as 673 K. The Zr^0 metallic surface state was confirmed on the Pd(111) surface by (i) almost no shift of the Pd $3d_{5/2}$ peak (peak position: 335.2 eV) and (ii) the fact that the Zr 3d intensity does not change following annealing (neither dissolution nor evaporation) and (iii) the shift of the Zr 3d binding energy toward 179.4 eV typical for metallic Zr species.[49,50] On the other hand, the interface between ZrO_x and the noble metal (Pd or Pt) likely plays an important role since this reduction is only working on Pd and Pt, but *e.g.* not on Cu, which is a less active material.

In order to extend our understanding of ZTB CVD under UHV to more realistic conditions, we compare the UHV results to the *in situ* XPS data obtained at the synchrotron radiation facility BESSY-II. Fig. 5 shows the Zr 3d spectra obtained during the *in vacuo* heating of the CVD grown ZrO_x film (~2000 L ZTB at 673 K, deposited amount ~0.6 ML) on Pd(111) and on polycrystalline Pd foil by the UHV-XPS (Omicron) and *in situ* by the NAP-XPS at BESSY II, respectively. The better vacuum conditions in the UHV-XPS set-up (5×10^{-11} mbar, water free) compared with the 5×10^{-8} mbar water-containing background in the NAP-XPS chamber allowed to obtain completely reduced zirconium. In *in situ* NAP-XPS, the highly reactive ZTB precursor was converted to mainly ZrO_2 right after preparation (Zr $3d_{5/2}$ at 182.4 eV). Also the amount of carbon is significantly lower in UHV-XPS, which we assign to enhanced precursor decomposition due to the intense synchrotron beam of the *in situ* experiment and partially to the high base pressure. In both experiments, heating in vacuum results in reduction: only metallic Zr (179.4 eV) was detected in UHV-XPS, whereas a larger fraction of "partially reduced" zirconium (interfacial species) is additionally observed in the *in situ* NAP-XPS experiment, as a Zr $3d_{5/2}$ component is found at *ca.* 181.0 eV. This state is assigned to an ultrathin layer of ZrO_2.[49] We tentatively assign this peak to oxygen-deficient and not fully metallic interfacial ZrO_xH_y, *e.g.* with metal–metal bonds to the Pd substrate and still remaining Zr–O–Zr entities to the outermost ZrO_2 layer(s). This may explain the suggested oxidation state between Zr^{4+} and Zr^0, but rather if *e.g.* a bi- or multilayered precursor would be affected by loss of interfacial oxygen between Zr and Pd.

The reduction of Zr^{4+} is more difficult in the NAP-XPS-System, as not all Zr can be fully reduced to the metallic state (Fig. 5). In the *ex situ* UHV experiment, where the reduction is fast and complete, no such partially reduced intermediates could be detected. This difference most likely arises from the much poorer vacuum conditions of the *in situ* NAP-XPS chamber as discussed above. The background pressure of any oxygen

containing molecules was, thus, found to be crucial for the eventual efficiency of Zr reduction. Also, the growth mode of the Zr^{4+} precursor species (*i.e.* layer thickness or island formation) may be already pre-determined by the residual gas conditions during deposition and/or annealing.

Upon further annealing ($T > 780$ K), dissolution of Zr into the Pd bulk occurs, leading to a significant loss of the Zr 3d intensity and the formation of a near-surface Pd–Zr alloy, as indicated by a slightly higher BE shift of the Pd 3d peaks (not shown herein). The BE of the dissolving Zr is found to be 179.6 eV, which is shifted about 0.2–0.4 eV towards higher BE from the position for bulk Zr^0.[50] The most likely reason is the enhanced Pd–Zr coordination in the subsurface regions, but charge-transfer processes and final state effects might also play a role.

3.1.3. Hydroxylation of surface Zr^0 species using water. The reduced state of Zr is heated to 723 K in 5×10^{-6} mbar and 0.3 mbar H_2O in the *ex situ* experiments and the *in situ* experiments, respectively. Hydroxylated zirconia, ZrO_xH_y, (Fig. 6, binding energy Zr $3d_{5/2}$ ~183.0 eV) and also a minor ZrO_2 component are detected in both experiments. In 5×10^{-6} mbar H_2O, the hydroxylation process is obviously slower because of a much lower H_2O pressure. At 723 K, hydroxylation mostly occurs within 15 min: the state assigned to interfacial Zr could be detected. Almost complete loss of Zr^0 and the associated highest degree of hydroxylation is reached after 30 min. Hydroxylation is faster and more complete in the *in situ* experiment (0.3 mbar) due to the higher H_2O pressure. The Zr $3d_{5/2}$ peak of hydroxylated Zr^{4+} differs from the fully oxidized state and is found at around 183.0 eV, which complies well with literature values.[51]

Only in the UHV *ex situ* experiment the hydroxylation process is fully reversible: annealing at 723 K fully re-establishes the metallic state of Zr. Most likely, the degree of reversibility of the reduction process is highly dependent on the background pressure of oxygen containing molecules such as H_2O and O_2 in the residual gas.

Even though a catalytic reforming cycle should rather involve reversibly formed hydroxyl groups at Zr sites, an analogous experiment can also be performed with O_2 instead of H_2O. Oxidative treatments in O_2 (*ex situ*) and 0.3 mbar O_2 (*in situ*) leads in both cases to fully oxidized ZrO_2. Oxidation in 5×10^{-7} mbar O_2 for the *ex situ* experiments is fast, after 10 min no more metallic Zr is found. Again, full reversibility to the Zr metal state is only achieved in the UHV chamber. Water-analogous results are also obtained for the *in situ* experiments with 0.3 mbar O_2 pressure. Here, again only partially reversible reduction is possible, highlighting the aforementioned limitations by the poorer background pressure.

3.1.4. DFT calculations of the initial stages of ZrO_2 reduction. To better understand the energetic pre-conditions leading to the pronounced reducibility of ultrathin ZrO_2 films on Pd surfaces, DFT calculations with variable ZrO_2 film thickness were performed. The reaction energy for deposition of a ZrO_2 film on the Pd(111) surface, as cut from the ZrO_2 bulk structure, is calculated by eqn (7) (see Section 2, ''Computational methods''). The corresponding reaction energies ΔE for 1 ML, 2 ML, and 3 ML thick ZrO_2 are 1.20, 1.14 and 1.20 J m^{-2}, indicating that the 2 ML ZrO_2 film is more stable than its 1 ML and 3 ML counterparts. The positive value of the reaction energy indicates that the process of cutting layers from the cubic ZrO_2 bulk structure and depositing them as an ultrathin ZrO_2 film on the Pd substrate is endothermic. To better understand the deposition of the ZrO_2 films, the reaction energy ΔE is separated into two parts, the formation energy ΔE_{film} of the respective ZrO_2 film from the bulk ZrO_2 structure, and the adsorption energy ΔE_{ads} of this film on the Pd substrate. Our calculations show that the formation of a freestanding ZrO_2 monolayer from the bulk structure would require an energy of 3.59 eV and an equilibrium lattice compressed by ~9%. The corresponding adsorption energy ΔE_{ads} for the 1 ML ZrO_2 film on the Pd substrate is −0.11 eV. Formation of a freestanding 2 ML ZrO_2 film from the bulk structure would require an energy of 5.09 eV and an equilibrium lattice compression of ~4%. The corresponding adsorption energy ΔE_{ads} for the 2 ML ZrO_2 film at the Pd(111) surface is −1.81 eV. To form a freestanding 3 ML ZrO_2 film from the bulk structure would require an energy of 5.66 eV and an equilibrium lattice compression of ~3%. The corresponding adsorption energy ΔE_{ads} for the 3 ML ZrO_2 film and Pd substrate is −2.18 eV. The lattice compression of ZrO_2 film with respect to the ideal bulk structure was observed in previous theoretical calculations.[52] With increasing thickness, the film lattice slowly approached the bulk lattice dimensions. It is noted that the 1 ML ZrO_2 film exhibits the smallest

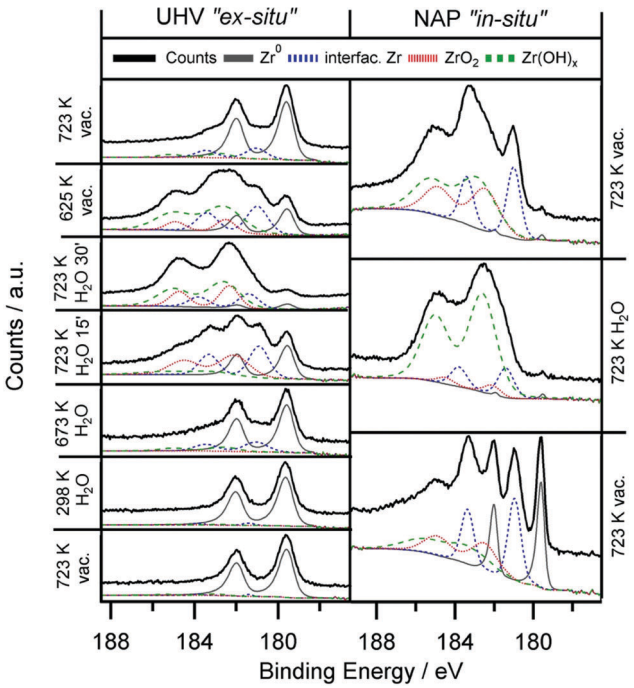

Fig. 6 Zr 3d spectra obtained *ex situ* and *in situ* during heating of 0.2 ML Zr^0/ZrO_xH_y in water. Zr^0/ZrO_xH_y is prepared by annealing of CVD-grown ZrO_xH_y (at 673 K, 2000 L ZTB) in $5 \times 10^{-11}/5 \times 10^{-8}$ mbar for the *ex situ* and *in situ* experiment, respectively. Left panels: *ex situ* UHV XPS experiments on Pd(111), water pressure 5×10^{-7} mbar. Right panels: *in situ* NAP-XPS experiments on a Pd foil, water pressure 0.3 mbar for 20 min.

adsorption energy, which is partially due to the strongest film reconstruction among the discussed 1–3 ML scenarios. In summary, the 3 ML ZrO_2 film is less stable than the 2 ML one due to the required larger film formation energy from the ZrO_2 bulk, and the 1 ML ZrO_2 film is less stable than the 2 ML one due to the smaller adsorption energy at the Pd substrate.

We then investigated three possible competing reactions for oxygen atom removal: to release $0.5O_2$ into the gas phase directly, to dissolve an O atom into the Pd sub-layer and to diffuse the O atom to the available neighboring bare Pd(111) surface. The free reaction energy at 725 K, calculated for an equilibrium pressure above the surface of $P_{O_2} = 10^{-12}$ mbar, is summarized in Table 1. Among the three possible competing reactions the interface oxygen diffusion to the neighboring bare Pd(111) surface is in any case the most favorable, followed by direct desorption into the gas phase as $0.5O_2$ and dissolution into the Pd sub-layer, which is the least favorable. The corresponding reaction energies for the interface-to-Pd oxygen diffusion are 0.74, 1.43, and 0.94 eV for the 1 ML, 2 ML and 3 ML thick ZrO_2 films, respectively, while the direct desorption of $0.5O_2$ into the gas phase is $\sim$0.20 eV higher than the diffusion. The corresponding reaction energies for oxygen dissolution in the Pd sub-layer amount to 2.00, 3.09 and 2.48 eV, which is in all cases much higher than the diffusion to the neighboring Pd(111) surface. We also found that the surface oxygen of the topmost layer and the interface oxygen of the lowest layer show the same reactivity for the direct O_2 desorption for the 1 ML and 2 ML ZrO_2 films. However, for the 3 ML ZrO_2 film, the interface oxygen is more active than the surface oxygen, indicating that the oxygen vacancy is more stable at the interface than at the outer surface. The corresponding structures for oxygen diffusion to the neighboring Pd(111) surface and dissolution into the sub-layer of the Pd substrate are shown in Fig. 7. As shown therein, the surface Pd atom moves up significantly by $\sim$0.40–0.50 Å in order to adapt the dissolved oxygen atom. In Table 1, we also included the movement of an interface Zr atom. As expected, atomic Zr dissolution from the interface to the Pd sub-layer is less favorable than atomic oxygen dissolution due to the large size of atomic Zr. The corresponding reaction energies are 2.78, 3.45 and 3.29 eV for the 1 ML, 2 ML, and 3 ML ZrO_2 films. Comparing all the reaction energies, it is noted that to move either O or Zr from the 2 ML ZrO_2 film is more difficult than that from the 1 ML and 3 ML films, suggesting that the 2 ML arrangement is the most stable one.

Table 1 Calculated reaction energy ΔG_{diss} (eV) of O/Zr dissolution into the Pd sub-layer, reaction Gibbs free energy ΔG_{O_2} (eV) of O_2 production in the gas phase, reaction energy ΔG_{diff} (eV) of O diffusion to the available neighboring bare Pd(111) surface at 725 K with $P_{O_2} = 10^{-12}$ mbar

ZrO_2	1 layer	2 layer	3 layer
$\Delta G_{diss}(O_{interface} \rightarrow O_{sub\text{-}layer/Pd})$	2.00	3.09	2.48
$\Delta G_{O_2}(O_{interface} \rightarrow 0.5O_2)$	0.94	1.63	1.14
$\Delta G_{O_2}(O_{surface} \rightarrow 0.5O_2)$	0.94	1.68	1.46
$\Delta G_{diff}(O_{interface} \rightarrow O_{Pd})$	0.74	1.43	0.94
$\Delta G_{diss}(Zr_{interface} \rightarrow Zr_{sub\text{-}layer/Pd})$	2.78	3.45	3.29

As discussed above, among the three possible competing reactions the interface oxygen rather prefers to diffuse to the available neighboring bare Pd(111) surface. Following this process, atomic oxygen may recombine to desorb as O_2 from the Pd surface. A number of previous experimental and theoretical studies have investigated O_2 adsorption/desorption on the Pd(111) surface.[53–57] Using thermal desorption spectrometry, one of our previous studies showed that the O_2 desorption rate from a chemisorbed O(ads) layer on Pd(111) reached its maximum at $\sim$750 K, which implies that associative O_2 desorption from bare Pd is both possible and irreversible under the UHV-reduction conditions chosen in the present study.[58]

The conclusions from this section regarding the optimum growth conditions for subsequent full reducibility are: (i) preferential single layer growth of ZrO_2 and (ii) a large phase boundary of the sub-monolayer ZrO_2 islands toward the surrounding bare Pd surface should be realized already during the deposition process.

3.2. Catalytic results

To correlate the redox chemistry of Zr on Pd with catalytic properties, the previously discussed Pd–Zr systems have been tested in two model reactions: methanol steam reforming and dry reforming of methane. While for the former no catalytically promoting role has been found (for an overview of the catalytic results, see ESI,† Section F, Fig. S4–S6), the latter is clearly promoted by Zr doping of Pd. These experiments, which show the opening of new CO_2 activation channels on Pd, are now discussed in Section 3.2.1.

3.2.1. Dry reforming of methane (DRM). To account for the eventual promoting role of Zr, the mixed valence $Pd/Zr^0/ZrO_xH_y$ model catalyst (again prepared by annealing of CVD grown ZrO_xH_y in vacuum), as well as the Pd : Zr = 2 : 1 intermetallic "IM" reference catalyst described in the experimental section, are tested for methane dry reforming (DRM, $CH_4 + CO_2 \rightarrow 2CO + 2H_2$). For this reaction, no initial water activation is required, but active sites both for CO_2 and CH_4 activation are mandatory. Water can in principle play a "co-catalytic" role as an intermediate or spoil the reaction as a side product, if CH_4 is not stoichiometrically converted and the inverse WGS reaction is active:

Water-free	Water-involving
$CH_4 \rightarrow C + 2H_2$	$CH_4 \rightarrow C + 2H_2$
$C + CO_2 \rightarrow 2CO$	$CO_2 + H_2 \rightarrow CO + H_2O$
	$C + H_2O \rightarrow CO + H_2$

The results of the DRM experiments are shown in Fig. 8. In none of the catalytic experiments shown therein, H_2O was detected, thus, at least the side reaction to water associated with the inverse WGS reaction is of minor importance. Carbon was detected with XPS on the surface after the reaction, but in too low amounts (relative to the gaseous reactant/product amounts) to affect the overall stoichiometry. Fig. 8 displays the DRM selectivity/activity pattern for a choice of "monofunctional"

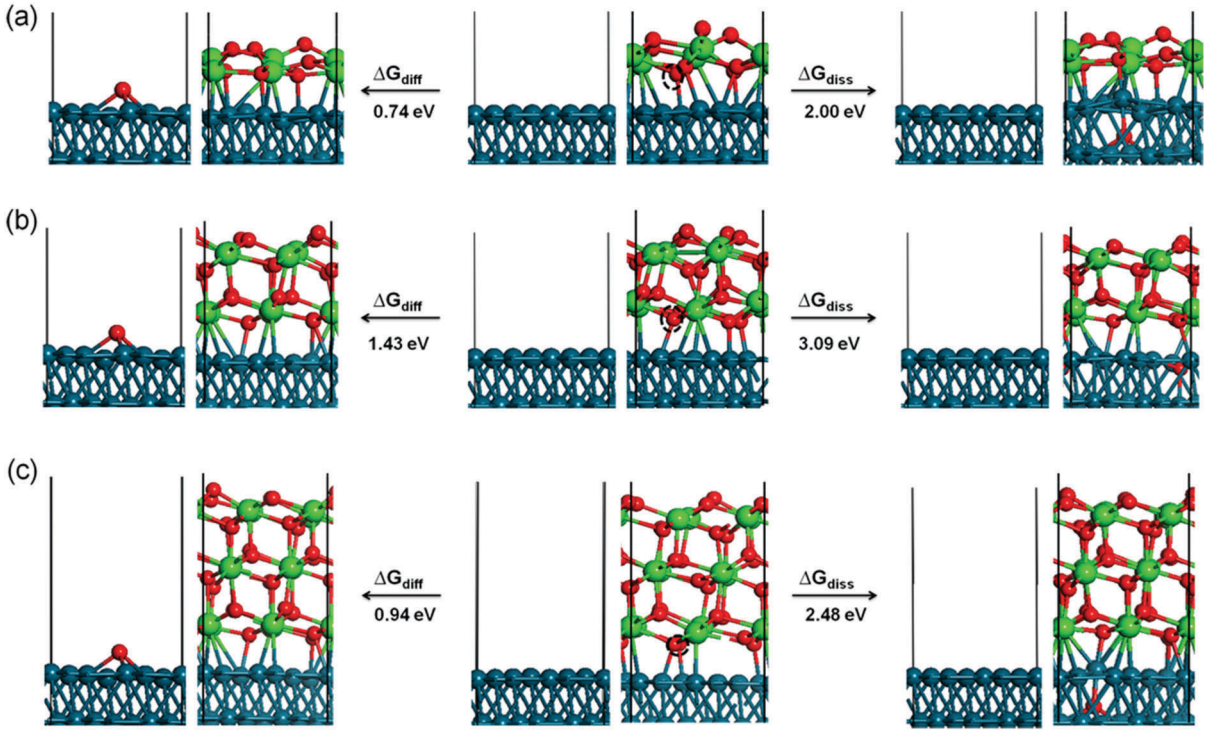

Fig. 7 Structural models of interface oxygen dissolution to the sub-layer of Pd(111) and diffusion to the available neighboring bare Pd(111) surface. The reaction energies are labeled. Left: the Pd–O diffusion scenario; right: dissolution scenario; middle: 1 (a), 2 (b), and 3 (c) ML ZrO_2 on the Pd(111) substrate. The moving O atom is marked by a dashed black circle. Small red spheres: O; large green spheres: Zr; blue spheres: Pd. The boxes indicate the computational supercell.

(pure Pd or Zr) and "bifunctional" (Pd–Zr) model catalysts. Clean Pd is completely inactive, as well as clean ZrO_2. Fig. 9 shows the corresponding XP spectra before and after selected DRM experiments of Fig. 8. A pure Zr metal foil was oxidized in 1 bar O_2 at 673 K to form a ZrO_2 layer that is thicker than the XPS analysis depth (95% of signal from topmost 5 nm for ZrO_2 with Mg Kα radiation). After the DRM reaction, the ZrO_2 film is reduced within the accessible information depth and a single state of Zr is detected in the XPS 3d region at a binding energy of 179.4 eV, which agrees well both with literature BE values of Zr^0[50] and zirconium carbide ZrC.[59] Destructive (sputter) depth profiling of this surface after catalysis is shown in the ESI† in Fig. S7, revealing a thickness of the carburized ZrC layer on top of Zr of at least 20 nm.

For the CVD-prepared and then vacuum- or oxygen-annealed $Pd/Zr^0/ZrO_xH_y$ or Pd/ZrO_2 samples, the activity in DRM depends on the initial oxidation state of Zr. As soon as there is a small fraction of Zr^0 available in the pre-catalyst (see arrow in Fig. 9), a measurable CO formation rate could be detected. In Fig. 8, the reaction rate is multiplied by a factor of 30 to show that there is some CO_2 consumed and CO formed at the stoichiometric ratio 1 : 2, but at a 30× lower rate as compared to the bulk-intermetallic "IM" catalyst described below. Again, no water side product formation could be detected. The temperature-programmed reaction profile for fully oxidized ZrO_2 on Pd (generated by annealing of the "as-grown" CVD layer in O_2 at 750 K) is not shown since no reactivity at all was detected, but the XP spectra for both ZrO_2 and ZrO_xH_y/Zr^0 on Pd are shown in Fig. 9 before and after DRM. On this basis, the fundamental activating function of Zr^0, which becomes *in situ* oxidized during DRM, could be shown qualitatively in spite of the very small initial Zr^0 amount. In order to substantiate this result, we decided to test an all-intermetallic bulk phase of Pd and Zr in the stoichiometry of 2 : 1 under otherwise identical DRM conditions ("IM" sample prepared by strongly exothermic co-melting, see chapter 2). The sample gets (surface) oxidized at room temperature over time, leading to a loss of Zr^0 in XPS (analysis depth ~2–3 nm). This oxidation was not found to be crucial for the catalyst performance. It does not matter whether Pd–Zr intermetallic is surface pre-oxidized in air at room temperature almost within the XPS analysis depth (Fig. 9). The "before DRM" – IM spectra in Fig. 9 shows the most air-oxidized state right before the catalytic experiment. Nevertheless, it shows residual Zr^0.

On this sample, the formation rate of CO is ~30 times higher than on the vacuum annealed CVD $Pd/Zr^0/ZrO_xH_y$ sample. This substantiates our interpretation that the (*in situ*) oxidative segregation from an initially intermetallic phase and/or surface leads to an enhanced number of reforming-active interfacial Pd/ZrO_xH_y sites. Again, we suggest the idea that the (*in situ*) oxidation of an atomically homogeneous intermetallic phase leads to the most disperse $Zr^{4+}O_xH_y$ surface-near distribution possible and therefore, to a maximum number of Pd/ $Zr^{4+}O_xH_y$ interface sites, *i.e.* to a quasi "atomically dispersed" phase boundary. The validity of this concept has

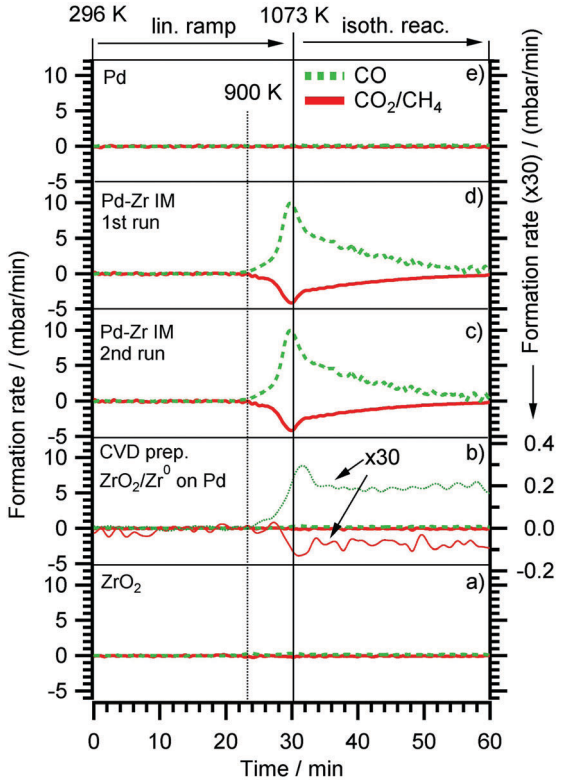

Fig. 8 Methane dry reforming (DRM) on (a) Clean oxidized Zr foil (identical with pattern for 0.3 ML ZrO_2 on Pd, prepared by post annealing of CVD grown ZrO_xH_y in 5×10^{-7} mbar O_2 at 700 K). (b) 0.3 ML Zr^0/ZrO_xH_y, prepared by annealing of CVD grown ZrO_xH_y in 5×10^{-9} mbar vacuum (the reactant consumption- and CO product formation rates were multiplied by a factor of 30 and plotted in the Y-scale range of the "IM" experiments (c and d) two consequent DRM runs of an intermetallic Pd : Zr = 2 : 1 "IM" bulk phase, (e) pure Pd. Initial DRM conditions: $CO_2 : CH_4$ = 1 : 1, total reactant pressure 100 mbar).

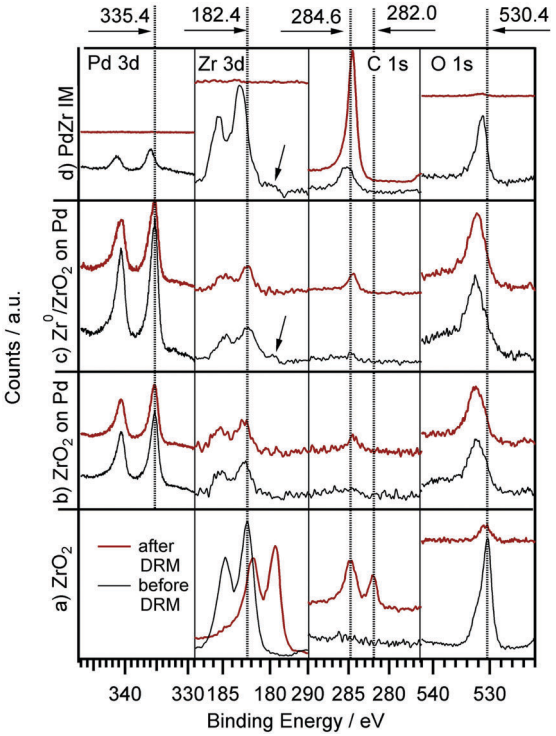

Fig. 9 XPS (Pd 3d, Zr 3d, C 1s and O 1s (overlapping with Pd 3p) region) before and after DRM experiments for: (a) clean Zr foil, pre-oxidized in 5×10^{-7} mbar O_2 at 750 K for 15 min; (b) 0.3 ML ZrO_2 on Pd, prepared by thermal annealing of CVD grown ZrO_xH_y in 5×10^{-7} mbar O_2 at 700 K; (c) 0.3 ML Zr^0/ZrO_xH_y, prepared by annealing of a CVD grown ZrO_xH_y in 5×10^{-9} mbar vacuum at 700 K; (d) intermetallic Pd/Zr (2 : 1) "IM" bulk phase before first and after second DRM run. The arrow indicates the Zr^0 component.

previously been proven for Cu/Zn[12], Pd/Zn[13] and Cu/Zr[11] and is now also confirmed for Pd/Zr. The enhanced DRM reactivity on the $Pd/Zr^0/ZrO_xH_y$ pre-catalyst is therefore mainly assigned to the synergistic action of very small Zr^0 clusters, which become partially oxidized and/or hydroxylated under reaction conditions and exhibit a high number of direct Pd neighbours. Obviously, the number of these desirable interfacial sites is even higher on the *in situ* oxidized IM bulk phase pre-catalyst, eventually leading to a 30 times higher reaction rate.

Note that no deactivation of the IM catalyst was found on the time scale of our experiments (2 × 60 min each, 1st and 2nd run). In both cases, the decrease of the reaction rate in the isothermal reaction section is due to complete consumption of CO_2 and CH_4, as the reactor is operated in re-circulating batch mode. This reproducibility and stability with respect to catalytic performance holds despite a huge amount of carbon deposition (or, possibly, surface segregation) after cooling in the reaction mixture (see C 1s region of uppermost panel in Fig. 9). The binding energy of ~284.5 eV and the rather large peak width (as compared to pure graphite) suggest a mix of sp^3- or sp^2-hybridized carbon species. The carbon layer is thick enough for complete shielding of both the Pd and Zr signals. This renders the absent deactivation of the catalyst after the first run even more surprising. Apparently, the catalytically active sites become again accessible during heating, *e.g.* if the carbon layer is reacted off by CO_2 and/or becomes re-dissolved in the bulk. Since the reaction sets in at ~900 K, the onset of the Boudouard reaction might explain this phenomenon. A final note on the bulk structure of the DRM-tested intermetallic Pd–Zr sample should be provided at this point. As already outlined in Section 2 and further elaborated upon in the discussion of Fig. S8 (ESI†), highlighting the X-ray diffractograms before and after the DRM reaction, despite the nominal 2 : 1 composition, the initial patterns reveal the presence of at least two intermetallic compounds with Pd excess, namely Pd_3Zr and Pd_4Zr_3. Upon performing the DRM reaction, the patterns get even more complex, including the complete removal of the Pd_3Zr phase and the formation of a new Pd_9Zr phase. Elementary, graphite-like carbon and partially oxidized ZrO_2 in the monoclinic and tetragonal modifications, formed by partial (oxidative) decomposition of the Pd–Zr intermetallic compounds, are equally observed. This is in striking contrast to Cu–Zr, where only one $Cu_{51}Zr_{14}$ compound was observed after preparation.[24] A common behavior (despite the different reactions) are the massive *operando* observed bulk structural changes accompanying the surface chemical alterations. However, due to the initially less homogeneous melt in the Pd–Zr case, the structural complexity is significantly more pronounced.

4. Conclusions

The CVD process of zirconium-*t*-butoxide ZTB was studied on Pd(111) single crystal and on polycrystalline Pd foil samples. A substrate temperature of ~700 K was found to be ideal to create a partially hydroxylated, carbon-depleted and vacuum-reducible ZrO_xH_y overlayer. Depending on the quality of the vacuum conditions, reversible partial or full reduction of the ZrO_xH_y overlayer (*i.e.* Zr^{4+}) to surface Zr^0 nanoclusters could then be accomplished. This very dynamic redox behaviour of ZrO_xH_y overlayers on Pd manifests itself in repeated oxidation (in water or oxygen) and vacuum-reduction cycles to the adsorbed Zr^0 metallic state without alloying up to 770 K. Nanoclusters of 2–6 Zr^0 atoms were found by STM if Pd/ZrO_xH_y was UHV-reduced at 723 K. DFT calculations show that the interfacial oxygen, especially that of a single-layer cubic ZrO_2 film, energetically prefers to diffuse to the available neighboring bare Pd(111) surface, rather than to desorb as O_2 or to become dissolved in the Pd subsurface region.

CVD-prepared and vacuum-reduced $Pd/Zr^0/ZrO_xH_y$ model catalysts are not MSR active up to 623 K, due to the formation of an interlayer of graphitic carbon between Zr and Pd, resulting in the loss of active Zr/Pd phase boundary sites. In contrast to the related Cu/ZrO_xH_y system, MSR on $Pd/Zr^0/ZrO_xH_y$ does, therefore, not proceed *via* the low (<623 K) temperature/partial dehydrogenation route with intermediate formaldehyde, which is thereafter totally oxidized by activated water to CO_2. On Zr-doped Pd, rather, the expected full dehydrogenation of methanol toward CO takes place on the bare Pd surface patches, followed by the (also water-activation dependent) water gas shift route toward CO_2 at higher temperatures above ~650 K. The latter process is only possible in the presence of an active Pd/ZrO_xH_y phase boundary, which is re-established above ~650 K by reactive removal of carbon deposits.

Dry reforming activity with almost 100% CO-selectivity is only observed if Zr^0 species either in a CVD-prepared/vacuum-reduced or melt-prepared intermetallic Pd–Zr "pre-catalyst" are initially present. With an intermetallic pre-catalyst bulk phase with a nominal 2 : 1 composition consisting of Pd^0 and Zr^0, the highest CO formation rates were obtained. At the surface of both systems, Zr^0 is not stable under DRM conditions, and $Zr^{4+}O_xH_y$ species are formed by *in situ* reactive oxidation/hydroxylation. This process is likely to lead to a particularly high number of active phase boundary sites. As discussed above, further studies will most likely be focused on identifying sophisticated synthesis routines, allowing to prepare single-phase Pd–Zr intermetallic compounds, whose intrinsic (catalytic) properties can, thus, be studied.

DFT calculations to describe the Pd/ZrO_xH_y induced CO_2 activation and the reaction mechanism to CO and H_2 are planned. Besides enhanced CO_2 activation, also formation of surface adsorbed carbon from CH_4 may be positively influenced by Pd/ZrO_xH_y. The present study provides phenomenological evidence for an enhanced phase boundary synergism, including a beneficial carbon chemistry. Thus, theoretical studies of the microscopic reaction mechanism at the active sites are imperative, since Zr doping of Pd obviously opens up special CO_2 activation pathways on chemically and electronically Pd, which are not available on clean undoped metallic Pd.

Acknowledgements

L. Mayr and Z. Shi acknowledge financial support *via* FWF SFB "FOXSI" project part F4503-N16, L. Mayr *via* a scholarship of the Carinthian Confederation of Industry (Industriellenvereinigung Kärnten). The computational results presented have been achieved (in part) using the Vienna Scientific Cluster (VSC). Support from the Department of Energy, Office of Basic Energy Sciences, Chemical Sciences, under Grant DE-FG02-03ER15408 is gratefully acknowledged. The authors acknowledge the Purdue Catalysis Center, We are grateful to Michael Detwiler, Amir Gharachorlou, Ronald G. Reifenberger and Fabio H. Ribeiro for many helpful suggestions and motivating discussions. We also thank the Birck Nanotechnology Center staff for their assistance and cooperation throughout. We gratefully acknowledge the Helmholtz-Zentrum-Berlin (HZB) for providing beamtime at the ISISS beamline.

References

1 K.-I. Fujimoto, F. H. Ribeiro, M. Avalos-Borja and E. Iglesia, *J. Catal.*, 1998, **179**, 431–442.
2 S. H. Liu, G. K. Chuah and S. Jaenicke, *J. Mol. Catal. A: Chem.*, 2004, **220**, 267–274.
3 D. He, Y. Ding, H. Luo and C. Li, *J. Mol. Catal. A: Chem.*, 2004, **208**, 267–271.
4 M. Behrens and M. Arnbrüster, Methanol Steam Reforming, in *Catalysis for Alternative Energy Generation*, ed. L. Guczi and A. Erdohelyi, Springer, New York, 2012, pp. 175–235.
5 P. Sudarsanam, B. Mallesham, P. S. Reddy, D. Großmann, W. Grünert and B. M. Reddy, *Appl. Catal., B*, 2014, **144**, 900–908.
6 W. Du, G. Zhao, H. Chang, F. Shi, Z. Zhu and X. Qian, *Mater. Charact.*, 2013, **83**, 178–186.
7 A. Atkinson, S. Barnett, R. J. Gorte, J. T. S. Irvine, A. J. McEvoy, M. Mogensen, S. C. Singhal and J. Vohs, *Nat. Mater.*, 2004, **3**, 17–27.
8 R. L. Puurunen, *J. Appl. Phys.*, 2005, **97**, 121301.
9 J. P. Chang, Y.-S. Lin, S. Berger, A. Kepten, R. Bloom and S. Levy, *J. Vac. Sci. Technol., B*, 2001, **19**, 2137–2143.
10 L. Mayr, N. Köpfle, A. Auer, B. Klötzer and S. Penner, *Rev. Sci. Instrum.*, 2013, **84**, 094103.
11 L. Mayr, B. Klötzer, D. Zemlyanov and S. Penner, *J. Catal.*, 2015, **321**, 123–132.
12 C. Rameshan, W. Stadlmayr, S. Penner, H. Lorenz, N. Memmel, M. Hävecker, R. Blume, D. Teschner, T. Rocha, D. Zemlyanov, A. Knop-Gericke, R. Schlögl and B. Klötzer, *Angew. Chem.*, 2012, **124**, 3057–3061.
13 C. Rameshan, W. Stadlmayr, C. Weilach, S. Penner, H. Lorenz, M. Hävecker, R. Blume, T. Rocha, D. Teschner, A. Knop-Gericke, R. Schlögl, N. Memmel, D. Zemlyanov,

G. Rupprechter and B. Klötzer, *Angew. Chem., Int. Ed.*, 2010, **49**, 3224–3227.
14 S. Wang, G. Q. Lu and G. J. Millar, *Energy Fuels*, 1996, **10**, 896–904.
15 P. Ferreira-Aparicio, A. Guerrero-Ruiz and I. Rodríguez-Ramos, *Appl. Catal., A*, 1998, **170**, 177–187.
16 H. Ay and D. Üner, *Appl. Catal., B*, 2015, **179**, 128–138.
17 N. H. Elsayed, N. R. M. Roberts, B. Joseph and J. N. Kuhn, *Appl. Catal., B*, 2015, **179**, 213–219.
18 F. Kertis, J. Snyder, L. Govada, S. Khurshid, N. Chayen and J. Erlebacher, *JOM*, 2010, **62**, 50–56.
19 M. Valden, X. Lai and D. W. Goodman, *Science*, 1998, **281**, 1647–1650.
20 A. Gharachorlou, M. D. Detwiler, X. K. Gu, L. Mayr, B. Klötzer, J. Greeley, R. G. Reifenberger, W. N. Delgass, F. H. Ribeiro and D. Y. Zemlyanov, *ACS Appl. Mater. Interfaces*, 2015, **7**, 16428–16439.
21 A. Gharachorlou, M. D. Detwiler, L. Mayr, X. K. Gu, J. Greeley, R. G. Reifenberger, W. N. Delgass, F. H. Ribeiro and D. Y. Zemlyanov, *J. Phys. Chem. C*, 2015, **119**, 19059–19072.
22 A. Gharachorlou, M. D. Detwiler, A. V. Nartova, Y. Lei, J. Lu, J. W. Elam, W. N. Delgass, F. H. Ribeiro and D. Y. Zemlyanov, *ACS Appl. Mater. Interfaces*, 2014, **6**, 14702–14711.
23 R. Paul, R. G. Reifenberger, T. S. Fisher and D. Y. Zemlyanov, *Chem. Mater.*, 2015, **27**, 5915–5924.
24 L. Mayr, D. Schmidmair, M. Armbrüster, N. Köpfle, J. Bernardi, S. Schwarz, B. Klötzer and S. Penner, *ChemCatChem*, 2016, **8**, 1778–1781.
25 L. Mayr, R. Rameshan, B. Klötzer, S. Penner and C. Rameshan, *Rev. Sci. Instrum.*, 2014, **85**, 055104.
26 A. Knop-Gericke, E. V. Kleimenov, M. Hävecker, R. Blume, D. Teschner, S. Zafeiratos and R. Schlögl, *Adv. Catal.*, 2009, **52**, 213–272.
27 *CasaXPS Version 2.3.16 Pre-rel 1.4*, Casa Software Ltd, 2011.
28 C. D. Wagner, W. M. Riggs, L. E. Davis, J. F. Moulder and G. E. Muilenberg, *Handbook of X-Ray Photoelectron Spectroscopy*, Perkin-Elmer Corporation, Physical Electronics Division, Eden Prairie, Minnesota, 1979, vol. 55344.
29 D. Majumdar and D. Chatterjee, *J. Appl. Phys.*, 1991, **70**, 988–992.
30 C. J. Powell and A. Jablonski, *NIST Electron Effective-Attenuation-Length Database SRD 82, Version 1.3*, Instititue of Standards and Technology, Gaithersburg, 2011.
31 J. J. Yeh, *Atomic Calculation of Photoionization Cross-Sections and Asymmetry Parameters*, Gordon and Breach Science Publishers, Langhorne, PE, USA, 1993.
32 G. Kresse and J. Furthmüller, *Phys. Rev. B: Condens. Matter Mater. Phys.*, 1996, **54**, 11169–11186.
33 G. Kresse and D. Joubert, *Phys. Rev. B: Condens. Matter Mater. Phys.*, 1999, **59**, 1758–1775.
34 J. Klimes, D. R. Bowler and A. Michaelides, *J. Phys.: Condens. Matter*, 2010, **22**, 022201.
35 J. Klimeš, D. R. Bowler and A. Michaelides, *Phys. Rev. B: Condens. Matter Mater. Phys.*, 2011, **83**, 195131.
36 X.-R. Shi, S.-G. Wang, J. Hu, Z. Qin and J. Wang, *Surf. Sci.*, 2012, **606**, 1187–1194.
37 J. P. Chang, Y.-S. Lin and K. Chu, *J. Vac. Sci. Technol., B*, 2001, **19**, 1782–1787.
38 M. A. Cameron and S. M. George, *Thin Solid Films*, 1999, **348**, 90–98.
39 H. Gabasch, E. Kleimenov, D. Teschner, S. Zafeiratos, M. Hävecker, A. Knop-Gericke, R. Schlögl, D. Zemlyanov, B. Aszalos-Kiss, K. Hayek and B. Klötzer, *J. Catal.*, 2006, **242**, 340–348.
40 C. T. Lynch, K. S. Mazdiyasni, W. J. Crawford and J. S. Smith, *Anal. Chem.*, 1964, **36**, 2332–2336.
41 I. Martinko, R. Verhoef, Y. Engelmann, J. Cornil, S. Salah, R. Snyders, O. Antonin and P. Raynaud, *22nd International Symposium on Plasma Chemistry*, 2015, vol. III, pp. 6–35.
42 R. Verhoef, P. Raynaud, S. Ligot, R. Snyders, T. Nelis, R. V. Gonzalez and S. Vitale, *21nd International Symposium on Plasma Chemistry*, 2013, p. OR 214.
43 Y. Sert, L. M. Singer, M. Findlater, H. Dogan and G. Cirak, *Spectrochim. Acta, Part A*, 2014, **128**, 46–53.
44 H. J. Oelichmann, D. Bougeard and B. Schrader, *J. Mol. Struct.*, 1981, **77**, 179–194.
45 H. J. Oelichmann, D. Bougeard and B. Schrader, *J. Mol. Struct.*, 1981, **77**, 149–163.
46 N. F. Brown and M. A. Barteau, *J. Am. Chem. Soc.*, 1992, **114**, 4258–4265.
47 M. W. Chase, *J. Phys. Chem. Ref. Data, Monogr.*, 1998, **9**, 1–1951.
48 J.-Q. Hu, M. Xie, Y. Pan, Y.-C. Yang, M.-M. Liu and J.-M. Zhang, *Comput. Mater. Sci.*, 2012, **51**, 1–6.
49 H. Li, J.-I. J. Choi, W. Mayr-Schmölzer, C. Weilach, C. Rameshan, F. Mittendorfer, J. Redinger, M. Schmid and G. Rupprechter, *J. Phys. Chem. C*, 2015, **119**, 2462–2470.
50 S. Sinha, S. Badrinarayanan and A. P. B. Sinha, *J. Less-Common Met.*, 1987, **134**, 229–236.
51 C. Huang, Z. Tang and Z. Zhang, *J. Am. Chem. Soc.*, 2001, **84**, 1637–1638.
52 K. Meinel, A. Eichler, S. Förster, K. M. Schindler, H. Neddermeyer and W. Widdra, *Phys. Rev. B: Condens. Matter Mater. Phys.*, 2006, **74**, 235444.
53 F. P. Leisenberger, G. Koller, M. Sock, S. Surnev, M. G. Ramsey, F. P. Netzer, B. Klötzer and K. Hayek, *Surf. Sci.*, 2000, **445**, 380–393.
54 Y. Cao and Z.-X. Chen, *Phys. Chem. Chem. Phys.*, 2007, **9**, 739–746.
55 M. Ji, C. Hao, Z. Xie, S. Liu and J. Qiu, *J. Comput. Theor. Nanosci.*, 2012, **9**, 394–400.
56 J. Klikovits, E. Napetschnig, M. Schmid, N. Seriani, O. Dubay, G. Kresse and P. Varga, *Phys. Rev. B: Condens. Matter Mater. Phys.*, 2007, **76**, 045405.
57 H. Gabasch, W. Unterberger, K. Hayek, B. Klötzer, G. Kresse, C. Klein, M. Schmid and P. Varga, *Surf. Sci.*, 2006, **600**, 205–218.
58 B. Klötzer, K. Hayek, C. Konvicka, E. Lundgren and P. Varga, *Surf. Sci.*, 2001, **482–485**, 237–242.
59 R. Kaufmann, H. Klewe-Nebenius, H. Moers, G. Pfennig, H. Jenett and H. J. Ache, *Surf. Interface Anal.*, 1988, **11**, 502–509.